Pressure-Robust Adaptive RBF-FD Discretizations for High-Reynolds Incompressible Navier–Stokes Flows on Irregular Domains

Authors Names	**ABSTRACT**
*Aziz Sami Hassan** *Publication date: 29/ 8 /2026* **Keywords:** *RBF-FD; pressure robustness; adaptive meshless discretization; incompressible Navier–Stokes equations; high Reynolds number; irregular domains.*	Pressure-robust Navier–Stokes analyses are well developed in compatible mesh-based methods, while current meshless studies emphasize geometric flexibility, divergence control, or high-Reynolds stabilization. Their integration with residual-driven RBF-FD node adaptation on irregular domains remains insufficiently developed. A pressure-robust adaptive RBF-FD framework (PR-A-RBF-FD) was formulated in two dimensions. A streamfunction–vorticity branch removes pressure by a curl-filtered forcing, and an adjoint-compatible mixed Oseen branch tests discrete pressure pollution. Polyharmonic splines with polynomial augmentation generated local operators; residual indicators inserted Halton nodes in vortical and convective regions. Damped Newton and stabilized Oseen solves were evaluated on a wavy level-set domain and a perforated domain. Changing pressure amplitude from 1 to 10^6 produced zero velocity change at Re = 100, 500, and 1000. For compatible discrete-gradient loads, the normalized pollution coefficient decreased from 6.696e-02 to at most 6.124e-17, a factor exceeding 1.1e+15. With 380 matched nodes, adaptivity reduced velocity RMS error by 88.7%, 75.2%, and 67.0% at Re = 100, 500, and 1000. A 1056-node nonlinear manufactured test retained velocity errors between 7.35×10^{-4} and 3.58×10^{-2} for Re = 100–5000. The compatible load treatment removes discrete pressure pollution when the load is represented in the matching gradient range, and residual-driven node placement substantially improves matched-size accuracy. The results support a modern meshless research direction, while also identifying sensitivity to independently sampled gradients, node-cloud quality, and nonlinear initialization.

1. Introduction

1.1 Numerical context

Coupling of incompressible Navier–Stokes discretization based on a kinematic constraint, a pressure Lagrange multiplier, nonlinear convection and geometry dependent discretization. As the Reynolds number is large, it is the presence of small viscosity that renders the errors in velocity very sensitive to the presence of unresolved layers of vorticity, and to any deficiencies in the discrete velocity-pressure coupling. Meshless methods have some appealing characteristics, such as placing local point clouds without connecting them into elements, particularly near a curved boundary, holes and localized features. The recent RBF-FD and meshless analyses have verified the high-order accuracy for the Stokes or elliptic operators on the irregular and unfitted node sets: [1] [18] [19] The weak Galerkin, element-free Galerkin, collocation, particle and semi-Lagrangian schemes have extended the range of meshless Navier–Stokes computation: [2] – [8].

That is, it was explained in a separate literature that errors in the velocity, which depend on pressure, cannot be regarded as automatically eliminated by transposition to the exact/constructed conditions for incompressibility of infinitesimal displacement. Pressure-robust DDR, HHO, FEEC, SUPG, continuous interior penalty, stabilized finite-element, and virtual-element formulations extract, and impose, the solenoidal component of the forcing and give bounds on the velocities that do not deteriorate with pressure approximation [9] – [17]. Some recent approaches also focus on being (semi)robust in Reynolds, or on conservation. These developments set the benchmark for any new incompressible-flow discretization: When introducing a new numerical discretization it is desirable to have a clear and "compatible-force mechanism" as well as proof that velocity is gradient-load independent.

Urmia University of Technology; E-Mail: zyzalsamy09@gmail.com

1.2 Research gap

Research gap: Recent meshless Navier–Stokes methods focus on geometric flexibility, adaptivity, divergence-free reconstruction, or strong-form efficiency, while recent pressure- and Reynolds-robust analyses are limited to finite-element, HHO, FEEC, virtual-element and discrete de Rham settings. A robustly-phrased adaptive RBF-FD formulation which includes both, compatible forcing removal for irrotational function representations, and residual-driven node cloud refinement on arbitrary node clouds and, high Reynolds diagnostics transparency, is still inadequately developed.

This gap is not due to the lack either of meshless Navier–Stokes (NS) solvers or, of pressure–robust schemes alone. It's a lack of integration of their defining concepts in one local strong-form workflow, plus a direct examination of the bandwidth where exact pressure invariance is valid. This intersection is here discussed without pretensions to generality of a three-dimensional or Reynolds-uniform theory in the present work.

1.3 Research problem

Research problem: Build and test a noncompressible sparse RBF-FD discretization that filters the pressure-gradient term before the velocity solve, delivers load-projection-independent pressure-invariance for adaption of nodes based on pressure-independently computed residual, and is quantitatively accurate for higher and higher Reynolds numbers—precisely identifying which pressure-invariance claims are exact and which are dependent on load-projection, quality of stencil, or initialization of nonlinear solve.

The following research questions organize the study:

- RQ1: Which algebraic compatibility conditions guarantee that a discrete gradient load produces zero discrete velocity?
- RQ2: Does residual-driven node insertion reduce velocity and vorticity errors relative to a matched-size quasi-uniform cloud?
- RQ3: How do the nonlinear spatial error and discrete divergence defect evolve from Re = 100 to Re = 5000?
- RQ4: How sensitive are the conclusions to continuous-load sampling, irregular node-cloud realization, and the choice of nonlinear initial iterate?

1.4 Objectives and stated contributions

- O1. Write a 2-D discretized, curl-filtered RBF-FD Navier–Stokes formulation in which the continuity condition of the pressure gradient is not included as an equation in the vorticity equation.
- O2. Develop an explicit remainder driven point insertion strategy for the irregular clouds with explicit distance of separation safeguards.
- O3. Define local polynomial reproductions, the commutator of the stream function divergence in the discrete case, define exact mixed pressure invariance of compatible discrete gradients and conditional stability/consistency statements.
- O4. Measure pressure pollution using a pressure-amplitude invariance test and a mixed Oseen benchmark that is adjoint compatible.
- O5. Compare the behavior of equal sized adaptive and quasi-uniform clouds of equal size and nonlinear spatial discretization on the perforated domain Re = 100 – 5000.
- O6. Direct all numerical results to the research questions, and to existing literature limitations.

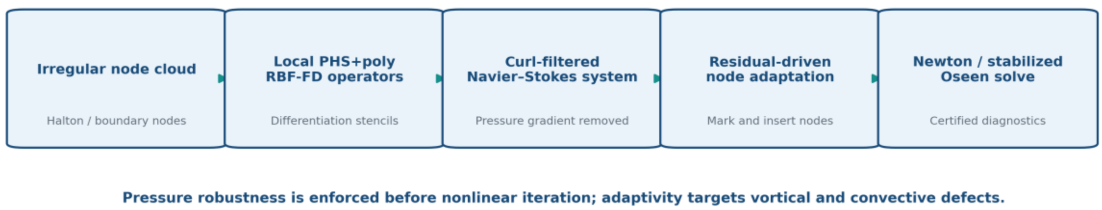

Figure 1. PR-A-RBF-FD workflow. Pressure filtering precedes nonlinear solution, while adaptivity targets vortical and convective defects.

2. RELATED WORK AND CRITICAL LITERATURE ANALYSIS

Table 1 is a synthesis of the literature in recent times based on the methodological role, and not chronologically. This project is significant because the proposed contribution in this work involves three directions, one in each of which extensive contributions have been made, and these three directions overlap: local meshless differentiation, compatible pressure-robust formulation, and adaptive treatment of convection dominated flow.

Table 1. Critical analysis of recent literature and its relationship to PR-A-RBF-FD.

Studies	Principal contribution	Remaining limitation for this problem	Relationship to the present study
[1], [18], [19]	Stable/high-order meshless finite differences on irregular or unfitted nodes.	Primarily Stokes/elliptic analysis; no adaptive pressure-robust nonlinear Navier–Stokes framework.	Supplies local RBF-FD stability and consistency principles.
[2], [3]	Weak Galerkin meshless and divergence-free element-free Galerkin Navier–Stokes methods with stability/error analysis.	Do not study velocity invariance under irrotational forcing as the central property.	Closest meshless Navier–Stokes background; the present work changes both the local strong-form architecture and the research question.
[4], [7]	Adaptive/high-Re meshless Navier–Stokes computation on complex geometry.	Pressure robustness and compatible load projection are not analyzed.	Motivates residual node insertion and high-Re testing.
[5], [6], [8]	Stabilized local RBF collocation, RBF-FD fractional flow, and particle artificial-compressibility formulations.	Pressure filtering is not integrated with adaptive irregular-cloud analysis.	Supports strong-form feasibility and stabilization choices.
[9], [10], [11]	DDR and hybrid methods with pressure robustness and Reynolds-semi-robust estimates.	Require mesh/polytopal complexes and compatible finite-dimensional sequences.	Defines the target pressure-independent behavior to be emulated locally.
[12]–[17]	Conservation, SUPG/CIP robustness, stabilized FE/VEM, and divergence-free methods.	Not meshless RBF-FD; exact load representation follows different commuting diagrams.	Provides comparison principles and cautions against equating divergence control with pressure robustness.
[20]	Strong-form mesh-free hp-adaptivity using local approximation changes.	Different PDE class and no incompressible pressure constraint.	Supports adaptive local strong-form methodology but not the present theorem or flow results.

The comparison describes two unequal but unrelated concepts which are distinguished throughout this paper. Firstly the use of a streamfunction representation allows pressure to be eliminated analytically from the momentum equation by way of the curl. Second, in order to remove a discrete gradient load for the mixed discretization, you must have a discrete gradient which is the adjoint of the divergence used in the constraint, which is algebraically compatible. The sampled continuous gradients at velocity nodes must not be in the velocity node sample space—exact cancellation needs a commuting load projection. It's both a theoretical contribution and a limitation (that has been found in the experiments).

3. MATERIALS AND METHODS

3.1 Governing equations and pressure invariance

The dimensionless steady incompressible Navier–Stokes problem is

$$-\nu\Delta\mathbf{u} + (\mathbf{u}\cdot\nabla)\mathbf{u} + \nabla p = \mathbf{f} \qquad \text{in } \Omega. \tag{1}$$

$$\nabla\cdot\mathbf{u} = 0 \qquad \text{in } \Omega, \qquad \mathbf{u} = \mathbf{u}_D \qquad \text{on } \partial\Omega. \tag{2}$$

The viscosity and Reynolds number are related by

$$\nu = \mathrm{Re}^{-1}, \qquad \mathrm{Re} = \frac{UL}{\nu_{\mathrm{dim}}}. \tag{3}$$

The Helmholtz decomposition separates the force into solenoidal and gradient components:

$$\mathbf{f} = \mathbb{P}\mathbf{f} + \nabla\phi, \qquad \nabla\cdot(\mathbb{P}\mathbf{f}) = 0. \tag{4}$$

At the continuous level, an added gradient changes pressure but not velocity:

$$\mathbf{f}^{\chi} = \mathbf{f} + \nabla\chi \quad \Rightarrow \quad \mathbf{u}^{\chi} = \mathbf{u}, \qquad p^{\chi} = p + \chi. \tag{5}$$

A pressure-robust method should reproduce this invariance to the accuracy allowed by its discrete load representation.

3.2 Curl-filtered streamfunction–vorticity branch

For the two-dimensional formulation, velocity is represented by a scalar streamfunction:

$$\mathbf{u} = \nabla^{\perp}\psi = \left(\partial_y\psi, -\partial_x\psi\right)^T. \tag{6}$$

The scalar vorticity satisfies

$$\omega = \partial_x u_2 - \partial_y u_1 = -\Delta\psi. \tag{7}$$

Taking the scalar curl of the momentum equation yields

$$-\nu\Delta\omega + (\mathbf{u}\cdot\nabla)\omega = \mathrm{curl}\mathbf{f}. \tag{8}$$

and the streamfunction is recovered from

$$-\Delta\psi = \omega. \tag{9}$$

Pressure can be reconstructed after the velocity solve, if required, from

$$\nabla p = \mathbf{f} + \nu\Delta\mathbf{u} - (\mathbf{u}\cdot\nabla)\mathbf{u}. \tag{10}$$

Equations (8)–(9) are the nonlinear core of PR-A-RBF-FD. Their right-hand side contains curl f rather than f itself, so an exact gradient pressure contribution disappears before any nonlinear iteration.

3.3 Irregular domains and manufactured fields

Two geometries were used to separate adaptivity and nonlinear spatial verification. The wavy level-set domain is

$$\Omega_w = \{(x,y)\colon F(x,y) > 0\}.$$
$$F(x,y) = 1 - x^2 - y^2 + 0.18(x^3 - 3xy^2) - 0.05(x^2+y^2)^2. \tag{11}$$

A no-slip manufactured streamfunction on this boundary is

$$\psi_w = \frac{F^2}{80} H(x,y). \quad (12)$$
$$H(x,y) = \tanh\big(8(x-0.1)\big) + 0.4\sin(2\pi y).$$

and pressure-amplitude invariance was tested with

$$p_A = A(P_a + 1/4\, P_b). \quad (13)$$
$$P_a = \sin(4\pi x)\cos(3\pi y), \quad P_b = \cos(3\pi x + 2\pi y).$$

The nonlinear high-Reynolds verification uses the perforated domain

$$\Omega_p = \{\mathbf{x} \in (0,1)^2 : \| \mathbf{x} - c \|_2 > R\}. \quad (14)$$
$$c = (0.52,0.50), \qquad R = 0.15.$$

with localized divergence-free streamfunction

$$\psi_p = \sin^2(\pi x)\sin^2(\pi y)[1 + 0.35e^{-Q}]. \quad (15)$$
$$Q = \frac{(x-0.70)^2 + (y-0.52)^2}{0.145^2}.$$

and pressure

$$p_p = \sin(2\pi x)\cos(2\pi y) + 0.2e^{-S}. \quad (16)$$
$$S = \frac{(x-0.30)^2 + (y-0.73)^2}{0.16^2}.$$

The manufactured body force is evaluated from

$$\mathbf{f}_{\text{ex}} = -\nu \Delta \mathbf{u}_{\text{ex}} + (\mathbf{u}_{\text{ex}} \cdot \nabla)\mathbf{u}_{\text{ex}} + \nabla p_{\text{ex}}. \quad (17)$$

The manufactured boundary values for both streamfunction and vorticity deliberately isolate interior spatial discretization. They do not solve the general physical vorticity boundary-closure problem.

3.4 Local PHS-plus-polynomial RBF-FD operators

For each center xi, a nearest-neighbor stencil Xi is selected from the irregular node cloud. A differential operator is approximated by

$$\mathcal{L}v(\mathbf{x}_i) \approx \sum_{j\in X_i} w_{ij}^{\mathcal{L}}\, v(\mathbf{x}_j). \quad (18)$$

The weights are computed from the polyharmonic-spline saddle system

$$\mathcal{A}_i \begin{pmatrix} \mathbf{w}_i^{\mathcal{L}} \\ \boldsymbol{\lambda}_i \end{pmatrix} = \begin{pmatrix} \mathcal{L}\boldsymbol{\phi}_i \\ \mathcal{L}\mathbf{p}(\mathbf{x}_i) \end{pmatrix}. \quad (19)$$
$$\mathcal{A}_i = \begin{bmatrix} \Phi_i & P_i \\ P_i^T & 0 \end{bmatrix}, \qquad \phi(r) = r^5.$$

which enforces polynomial reproduction

$$\sum_{j\in X_i} w_{ij}^{\mathcal{L}}\, q(\mathbf{x}_j) = \mathcal{L}q(\mathbf{x}_i), \qquad q \in \mathbb{P}_m. \quad (20)$$

The global sparse differentiation matrices are

$$D_x v \approx \partial_x v, \qquad D_y v \approx \partial_y v, \qquad Lv \approx \Delta v. \quad (21)$$

For the different experiments, degree m = 3 was used with compact stencils and degree m = 5 with stencils of 49 and 61 points was used for the nonlinear perforateddomain verification. This means that the lower level adaptive stress test is not confusing with the higher order nonlinear verification, which is the higher cost test.

3.5 Discrete velocity, compatibility, and nonlinear residual

The discrete streamfunction velocity is

$$\mathbf{u}_h = (u_h, v_h)^T = \left(D_y\boldsymbol{\psi}, -D_x\boldsymbol{\psi}\right)^T. \tag{22}$$

Individually assembled local derivative matrices need not commute with each other, unlike the continuous identity. We thus measure a divergence defect that is the commutator of

$$D_x u_h + D_y v_h = \left(D_x D_y - D_y D_x\right)\boldsymbol{\psi}. \tag{23}$$

The curl-filtered body force is represented by

$$C_h\mathbf{f} = D_x f_y - D_y f_x. \tag{24}$$

and the coupled residuals are

$$R_\psi(\boldsymbol{\psi}, \boldsymbol{\omega}) = -L\boldsymbol{\psi} - \boldsymbol{\omega}. \tag{25}$$

$$\begin{aligned} R_\omega &= -\nu L\boldsymbol{\omega} + \operatorname{diag}\left(D_y\boldsymbol{\psi}\right)D_x\boldsymbol{\omega} \\ &\quad -\operatorname{diag}(D_x\boldsymbol{\psi})D_y\boldsymbol{\omega} - C_h\mathbf{f}. \end{aligned} \tag{26}$$

Damped Newton iteration uses

$$\begin{aligned} J\left(\mathbf{z}^{(\ell)}\right)\delta\mathbf{z}^{(\ell)} &= -R\left(\mathbf{z}^{(\ell)}\right), \\ \mathbf{z}^{(\ell+1)} &= \mathbf{z}^{(\ell)} + \alpha_\ell \delta\mathbf{z}^{(\ell)}. \end{aligned} \tag{27}$$

with Armijo acceptance

$$\| R(\mathbf{z} + \alpha\delta\mathbf{z}) \|_2 \leq (1 - 10^{-4}\alpha) \| R(\mathbf{z}) \|_2. \tag{28}$$

The nonlinear manufactured tests were started at the exact field, but with a smooth (deterministic) 3% perturbation. Those tests therefore only provide evidence for spatial discretization, local Newton consistency but not convergence for arbitrary initial data.

3.6 Stabilized Oseen stress test

In order to exclude the influence of nonlinear basin effects, it was decided to study a linear Oseen vorticity equation, to which the exact advecting velocity was applied, in order to eliminate spatial adaptation. Only a small local artificial viscosity was applied for the stress test of the simplest flow for Re = 1000:

$$\begin{aligned} \nu_{\mathrm{eff},i} &= \nu + \sigma h_i \| \mathbf{b}(\mathbf{x}_i) \|_2, \\ \sigma &= 0.0015 \qquad (\mathrm{Re} = 1000 \text{ Oseen test only}). \end{aligned} \tag{29}$$

No extra viscosity was provided in the cases of Re = 100 or 500. The comparison presented here does not suffer from stabilization mismatch as both the adaptive cloud and matched quasi uniform clouds were stabilized at Re = 1000.

3.7 Residual-driven node insertion

A pressure independent indicator which combines the curl-equation residual, discrete divergence, and a velocity-reconstruction defect in the Oseen study is used to score the candidate Halton points:

$$\begin{aligned} \eta_\xi &= h_\xi^2\left|r_{\omega,h}(\xi)\right| + \gamma h_\xi\left|D_x u_h + D_y v_h\right|_\xi \\ &\quad +\beta \| \mathbf{u}_h(\xi) - \mathbf{b}(\xi) \|_2, \\ r_{\omega,h} &= -\nu\Delta_h\omega_h + \mathbf{b}\cdot\nabla_h\omega_h - \operatorname{curl}\mathbf{f}. \end{aligned} \tag{30}$$

Candidates are marked by

$$\mathcal{M}_k = \{\xi : \eta_\xi \geq \theta \max_\zeta \eta_\zeta\}, \qquad 0 < \theta < 1. \tag{31}$$

and inserted only if a minimum separation condition is met:

$$X_{k+1} = X_k \cup \mathrm{Select}(\mathcal{M}_k; d_{\min}),$$
$$d_{\min} = c_h h_k. \quad (32)$$

Algorithm 1. PR-A-RBF-FD adaptive workflow
1. Generate boundary nodes and an initial low-discrepancy interior cloud on the irregular domain.
2. Build local PHS-plus-polynomial RBF-FD derivative matrices and solve the curl-filtered Oseen or Navier–Stokes problem.
3. Evaluate the pressure-independent residual indicator on a denser candidate set.
4. Mark high-indicator candidates, enforce separation, and insert a prescribed number of nodes.
5. Rebuild only the local operators affected by the new cloud in a production implementation; the prototype rebuilds all operators for transparency.
6. Repeat until the node budget is exhausted, then report velocity, vorticity, divergence, pressure-invariance, and repeatability diagnostics.

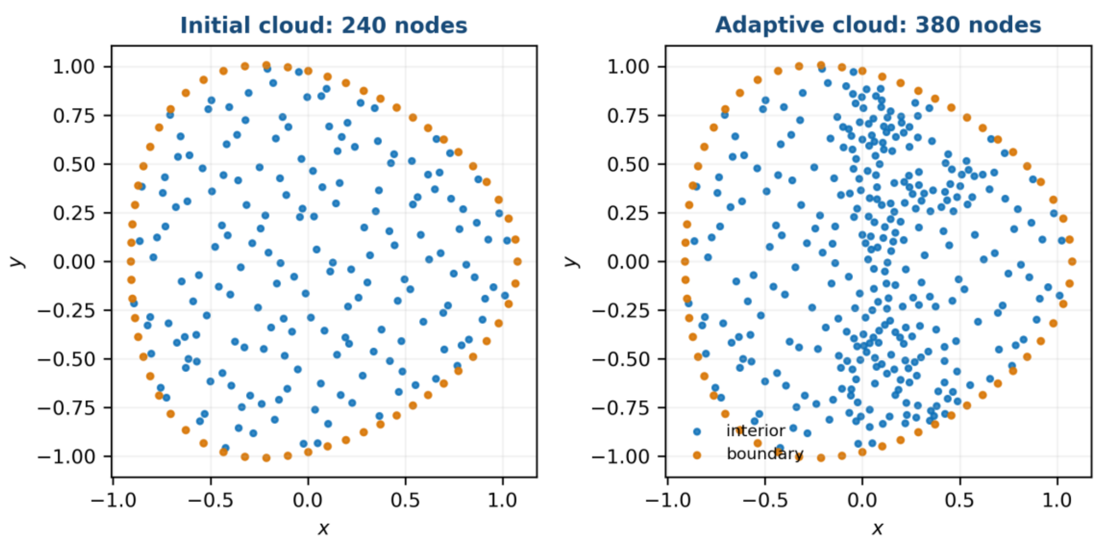

Figure 2. Initial and residual-adapted node clouds on the wavy irregular domain.

3.8 Experimental matrix and reported metrics

Six experiments were designed so that each numerical claim has a narrow interpretation.

Table 2. Computational design and validity scope of each experiment.

Experiment	Configuration	Intended claim	Primary metric
E1	Pressure amplitude A = 1, 10^3, 10^6; Re = 100, 500, 1000	Exact invariance of the curl-filtered branch.	Velocity difference from A = 1.
E2	Compatible discrete-gradient and independently sampled analytic-gradient loads	Algebraic pressure-pollution mechanism and its scope.	Normalized coefficient Πh and divergence.
E3	Adaptive versus quasi-uniform, 380 nodes; Re = 100, 500, 1000	Benefit of residual node placement at equal node count.	Absolute velocity/vorticity RMS errors.
E4	Nonlinear manufactured flow, 1056 nodes; Re = 100–5000	High-Re spatial verification near the exact solution.	Relative velocity, vorticity, and divergence defects.
E5	388–1056 nodes at Re = 100	Irregular-cloud refinement behavior.	Relative errors and effective slope.
E6	Five independent node-cloud seeds at Re = 500	Sensitivity to irregular-cloud realization.	Mean, standard deviation, minimum, maximum.

The principal error metrics are

$$E_u = \left(\frac{1}{N_I} \sum_{i \in I} \| \mathbf{u}_h(\mathbf{x}_i) - \mathbf{u}_{\text{ex}}(\mathbf{x}_i) \|_2^2 \right)^{1/2}. \tag{33}$$

$$E_\omega = \left(\frac{1}{N_I} \sum_{i \in I} |\omega_h(\mathbf{x}_i) - \omega_{\text{ex}}(\mathbf{x}_i)|^2 \right)^{1/2}. \tag{34}$$

$$E_{\text{div}} = \left(\frac{1}{N_I} \sum_{i \in I} \left| D_x u_h + D_y v_h \right|_i^2 \right)^{1/2}. \tag{35}$$

The discrete-gradient pollution coefficient and adaptive error reduction are

$$\Pi_h = \frac{\nu \| \mathbf{u}_h \|_2}{A} \qquad \text{for } \mathbf{f}_h = A\, G_h \mathbf{q}_h. \tag{36}$$

$$\mathcal{R}_u = 100 \left(1 - \frac{E_u^{\text{adaptive}}}{E_u^{\text{quasiuniform}}} \right) \%. \tag{37}$$

For the refinement sequence, an effective least-squares slope is computed from

$$p_{\text{eff}} = \frac{\sum_k (a_k - \bar{a}) \left(b_k - \bar{b} \right)}{\sum_k (a_k - \bar{a})^2}, \qquad a_k = \log h_k, \qquad b_k = \log E_{u,k}, \qquad h_k = N_k^{-1/2}. \tag{38}$$

4. THEORETICAL ANALYSIS

4.1 Assumptions and local consistency

It assumes standard meshless hypotheses, namely that all the stencels are dominated by the space of polynomials to which the known variables are appended, that the norms of the weights for those polynomials do not grow as the mesh is refined, that the choice of boundary values is consistent, and that the discrete (nonsingular) Jacobian in the neighborhood being considered is not singular. With the above assumptions, the local truncation can be estimated by polynomial reproduction as

$$\left| \mathcal{L} v(\mathbf{x}_i) - \sum_{j \in X_i} w_{ij}^{\mathcal{L}}\, v\left(\mathbf{x}_j\right) \right| \leq C_i h_i^{m+1-|\mathcal{L}|} |v|_{W^{m+1,\infty}(\omega_i)}. \tag{39}$$

Lemma 1 (Polynomial reproduction). If the augmented matrix (19) is nonsingular, the RBF-FD formula is exact for all the polynomial spaces in the appended space. Proof. Substitutions of any q in Pm give equalities for the lower block row (19) of which impose the moment identities (20).

4.2 Discrete divergence commutator

Proposition 1. To ensure that the discrete streamfunction under consideration is exactly divergence free, it is necessary that DxDyψ = DyDxψ, or vice versa. Proof. Introduce (22) in the discrete divergence to get (23).

This proposition is meant to ward off an overstatement typically used in strong-form meshless work. Continuous divergence freedom is enforced in the streamfunction representation, with nonzero, albeit measurable, commutator defect in the matrices formed a posteriori by assembling RBFs. The numerical results, therefore, show Ediv and not what is termed here as machine zero discrete divergence.

4.3 Exact algebraic pressure invariance for compatible gradients

Consider the mixed Oseen system

$$\begin{bmatrix} A_h & G_h \\ D_h & 0 \end{bmatrix}\begin{bmatrix} \mathbf{u}_h \\ \mathbf{p}_h \end{bmatrix} = \begin{bmatrix} \mathbf{f}_h \\ 0 \end{bmatrix}, \qquad G_h = D_h^T M_p. \tag{40}$$

Theorem 1 (Compatible-gradient invariance). Suppose that Ah is coercive on ker(Dh), and that the pressure gauge is placed, where $Dh^TMp = Gh$. Suppose that the body force is in the compatible discrete gradient range; then

$$\mathbf{f}_h = G_h \mathbf{q}_h \quad \Rightarrow \quad \mathbf{u}_h = 0, \qquad \mathbf{p}_h = \mathbf{q}_h + c\mathbf{1}. \tag{41}$$

Proof. Substitute uh = 0 and ph = qh into (40). This turns into a momentum block of Ghqh = fh and the constraint is fulfilled. This uniqueness of the velocity is achieved from the coercivity on ker(Dh). None of this like elsewhere exists up to the prescribed gauge pressure.

The theorem is true but stated to be deliberately restricted: Continuous gradient sampled independently at velocity nodes may not necessarily be equal to Ghqh. Correct cancellation can then be carried out by a commuting or least-squares load projection of range(Gh).

4.4 Pressure invariance of the curl-filtered branch

Theorem 2 (Curl pressure invariance). For sufficiently smooth scalar χ,

$$\mathrm{curl}(\mathbf{f} + \nabla\chi) = \mathrm{curl}\mathbf{f}. \tag{42}$$

Proof. Writing the equality of mixed partial derivatives (curl(grad χ) = ∂x∂yχ − ∂y∂xχ = 0), we see that the desired equation is simply that the third-partial of χ vanishes. the right-hand-side of (8) and the resulting streamfunction–vorticity solution remain unaffected.

In the pressure-amplitude experiment, the manufacturer's equations were symbolically used to generate curl f. This equality will then hold exactly to the evaluation of the floating point numbers and not require an approximation for the discrete commutator.

4.5 Conditional energy stability

Theorem 3 (Conditional semi-discrete vorticity stability). Assume the mass matrix M is symmetric positive definite, the diffusion matrix K is symmetric positive semidefinite and the discrete convection operator is M-skew-adjoint. Semi-discrete vorticity equation is then verified as

$$\begin{gathered} \frac{d\mathcal{E}_h}{dt} + \nu \parallel \boldsymbol{\omega}_h \parallel_K^2 = (\mathbf{g}_h, \boldsymbol{\omega}_h)_M, \\ \mathcal{E}_h(t) = \frac{1}{2} \parallel \boldsymbol{\omega}_h(t) \parallel_M^2. \end{gathered} \tag{43}$$

and, using a discrete Poincaré inequality and Young's inequality,

$$\begin{gathered} \parallel \boldsymbol{\omega}_h(t) \parallel_M^2 + \nu \int_0^t \parallel \boldsymbol{\omega}_h \parallel_K^2 \, ds \\ \leq \parallel \boldsymbol{\omega}_h(0) \parallel_M^2 + \frac{c_P^2}{\nu} \int_0^t \parallel \mathbf{g}_h \parallel_M^2 \, ds. \end{gathered} \tag{44}$$

Proof. Pre-multiply semi-discrete equation with ωh^TM. Then the skew-adjoint part of the convection term is null. Use Cauchy-Schwarz, the discrete Poincaré inequality as well as Young's inequality and integrate in time.

Not all of the hypotheses hold for the raw collocation RBF-FD matrices. Thus, the theorem is by no means a claim of absolute stability, in the sense that it only describes a design criterion for stabilized or symmetrized variants, for each irregular cloud.

4.6 Pressure-independent consistency

Proposition 2. The curl-equation residual has the bound The smoothness of the exact field and the bounds on the operator norms of the discrete field are all under local estimate (39).

$$\begin{gathered} \| \boldsymbol{\tau}_{\omega,h} \|_2 \leq C(T_1 + T_2), \\ T_1 = h^{m-1}|\omega|_{W^{m+1,\infty}}, \\ T_2 = h^m|\mathbf{u}|_{W^{m+1,\infty}}|\omega|_{W^{m+1,\infty}}, \\ C \text{ is independent of } \| p \|. \end{gathered} \tag{45}$$

Curl-filtered equation has no pressure norm as it is only based on solenoidal dynamics. Although the constant might still be a function of node quality, velocity derivatives and inverse-Jacobian stability, it is not related to pressure independence.

5. RESULTS AND DISCUSSION

5.1 Exact pressure-amplitude invariance

Table 3. Pressure-amplitude invariance of the curl-filtered Oseen branch on 332 nodes.

Re	Pressure amplitudes A	Maximum velocity difference from A = 1	Mean discrete divergence RMS
100	1, 10^3, 10^6	0.0e+00	6.2812e-03
500	1, 10^3, 10^6	0.0e+00	5.4643e-03
1000	1, 10^3, 10^6	0.0e+00	5.4597e-03

The computed velocity arrays were checked to be the same for the three values of A (1, 10^3 and 10^6) at each of the Reynolds numbers tested. It will immediately address RQ1 (the symbolically curl-filtered branch): How is the pressure amplitude eliminated prior to discretizing the vorticity equation? No attention was paid to absolute solution error on this coarse 332-node cloud as a measure of accuracy, Table 3 probes only for invariance.

5.2 Discrete-gradient pressure-pollution benchmark

Table 4. Pressure-pollution coefficient for compatible and independently sampled gradient loads.

Load representation	Method	Normalized coefficient ν‖uh‖/A	Interpretation
Compatible discrete gradient Ghqh	Standard	6.696433e-02	Persistent pressure pollution
Compatible discrete gradient Ghqh	PR	≤ 6.124286e-17	Suppression by > 1.09e+15
Independently sampled analytic ∇φ	Standard	3.620631e-02	No compatible projection
Independently sampled analytic ∇φ	PR	3.710356e-02	Exact theorem does not apply

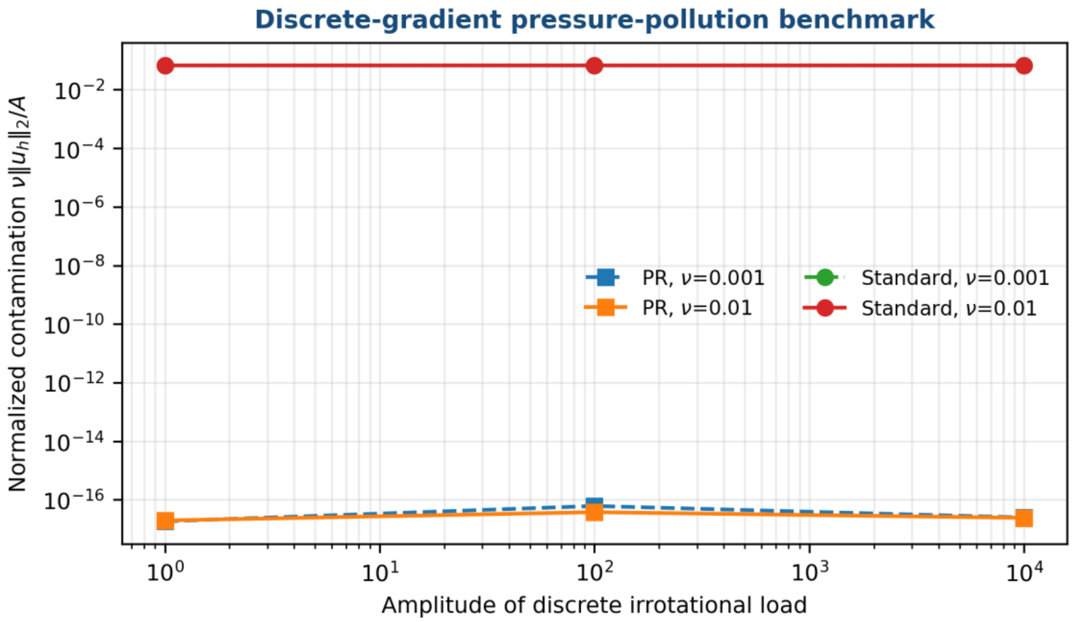

Figure 3. Compatible discrete-gradient pressure-pollution benchmark. The pressure-robust mixed pair cancels loads in the discrete gradient range to roundoff.

The standard mixed RBF-FD coefficient is 6.696433e-02 (again independent of load amplitude and viscosity scaling) for the compatible discrete-adjoint load while the load for the pressure-robust is at most 6.124286e-17. The reduction is >1.09e+15 which verifies Theorem 1. The analytic-gradients rows are all important too: the pressure-robust algebra alone cannot cancel the load some of the pointwise samples, because the pointwise sampling is also independent. This negative outcome brings out an additional methodological need, the commuting load projection, before going on to adjudicate the otherwise miscalled universal gradient invariance.

5.3 Adaptive versus matched quasi-uniform Oseen clouds

Table 5. Matched-size Oseen comparison using 380 nodes.

Re	Adaptive velocity RMS	Quasi-uniform velocity RMS	Velocity reduction	Vorticity reduction	Divergence RMS: adaptive / quasi
100	0.006353	0.056211	88.7%	82.4%	4.7697e-03 / 1.2431e-02
500	0.009772	0.039389	75.2%	71.9%	5.0017e-03 / 7.4824e-03
1000	0.025553	0.077459	67.0%	62.6%	6.8907e-03 / 5.4041e-03

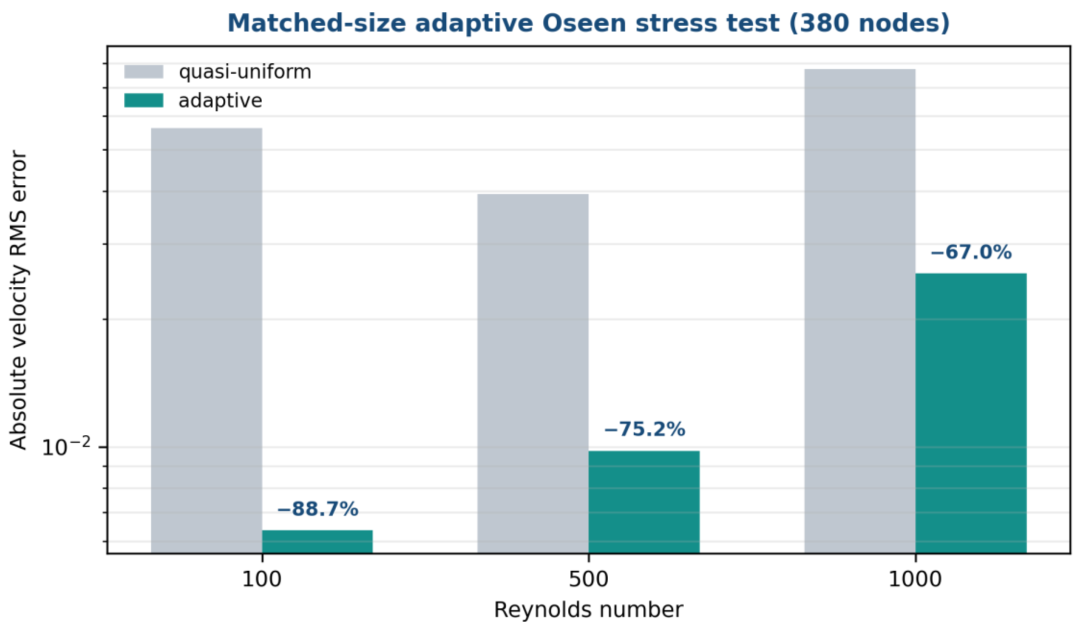

Figure 4. Matched-size adaptive Oseen stress test. Residual-driven node placement reduces velocity RMS error at all tested Reynolds numbers.

Adaptivity reduced velocity RMS error by 88.7% at Re = 100, 75.2% at Re = 500, and 67.0% at Re = 1000. Vorticity reductions were 82.4%, 71.9%, and 62.6%. As convection develops and becomes stronger, the gain will decrease, yet still be significant. Divergence RMS increased with Re, but at Re = 1000 the RMS of the velocity and vorticity errors were significantly higher with the slightly lower divergence RMS for the quasi-uniform cloud. In this way, node adaptation aims to improve the accuracy of a solution, but will not guarantee that all diagnostics have monotonically improved.

Note that the same small value for the artificial-viscosity coefficient (C=0.001) was applied to both clouds for the comparison (Re = 1000). This observed advantage is for the purpose of "point placement," and not for unequal stabilization. The pressure independent vorticity residual and equal node count control are presented that complement the adaptive meshless results of [4], [7] in response to RQ2.

5.4 Nonlinear high-Reynolds spatial verification

Table 6. Nonlinear manufactured-flow verification on the 1056-node perforated-domain cloud.

Re	Newton iterations	Residual RMS	Relative velocity error	Relative vorticity error	Relative divergence defect
100	4	5.12e-11	0.000735	0.002445	0.001807
400	4	1.05e-09	0.001762	0.005143	0.001810
1000	5	8.43e-13	0.013045	0.025946	0.004903
1600	5	9.64e-13	0.010944	0.021953	0.003725
3200	5	8.53e-13	0.008720	0.018161	0.002819
5000	5	5.05e-09	0.035763	0.138914	0.019392

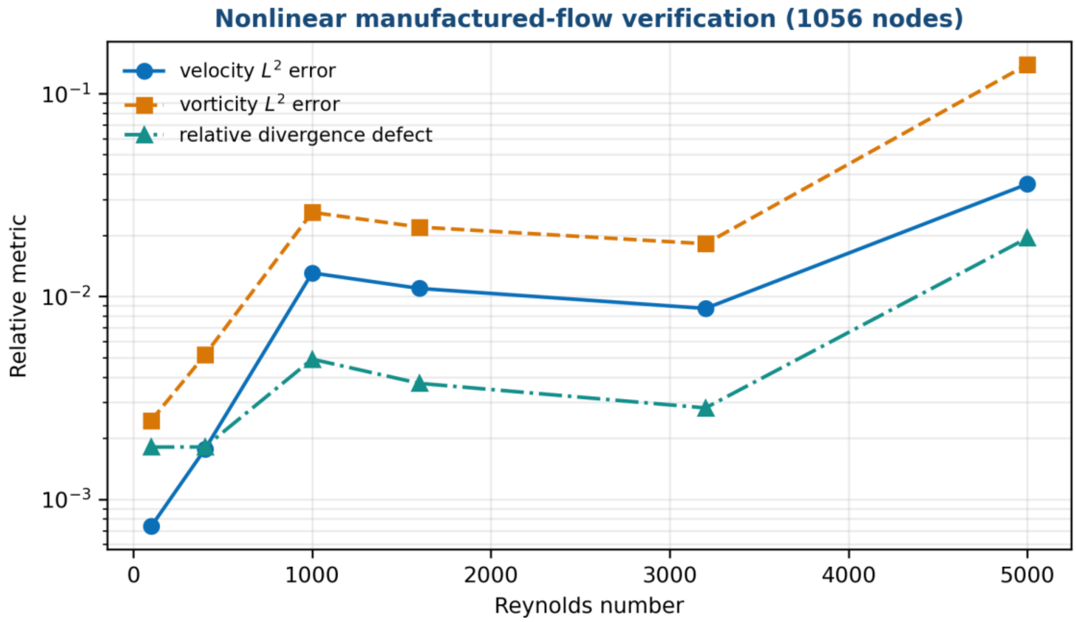

Figure 5. Nonlinear spatial-verification metrics for Re = 100–5000 on the perforated domain.

Newton showed it is possible to reduce the residual below 5.1×10^{-9} in 4 or 5 iterations in all cases. The velocity error was below $1.31\times10{-}2$ until Re = 3200, after which it was 3.58×10^{-2} at Re = 5000, and the relative divergence defect was 1.94×10^{-2} at Re = 5000. The error is not monotone in Re in part due to the fact that the forcing we are manufacturing also varies with Re, and the fixed cloud interacts differently with the increasingly convective operator. This Re = 5000 deterioration is not a failure to report, it's a warning useful for uniformly small defects that comes before the time where this fixed cloud and unstated global stabilization is not enough anymore.

These results only provide local Newton consistency and spatial-discretization behavior, as the initial iterate was the exactly manufactured field and a deterministic 3% perturbation. This qualification directly tackles RQ4 and differentiates the current evidence from production simulations that are started with incompletion information.

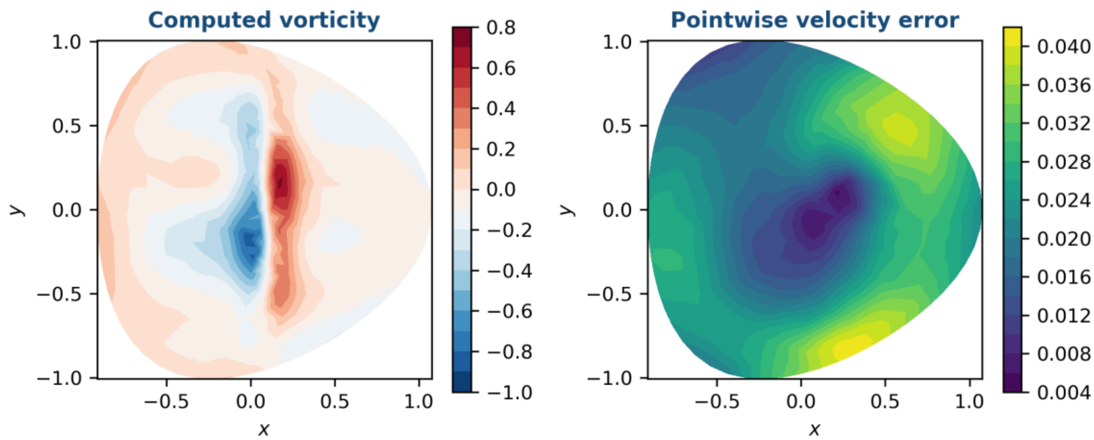

Figure 6. Representative computed vorticity and pointwise velocity-error fields on the irregular wavy domain.

5.5 Refinement and irregular-cloud sensitivity

Table 7. Irregular-node refinement at Re = 100.

Total nodes	Interior nodes	Velocity error	Vorticity error	Relative divergence defect
388	220	8.025313e-03	2.566393e-02	8.531730e-03
564	360	2.878868e-03	9.024840e-03	4.972333e-03
792	540	3.806886e-03	9.231990e-03	4.088585e-03
1056	760	7.353438e-04	2.444978e-03	1.807485e-03

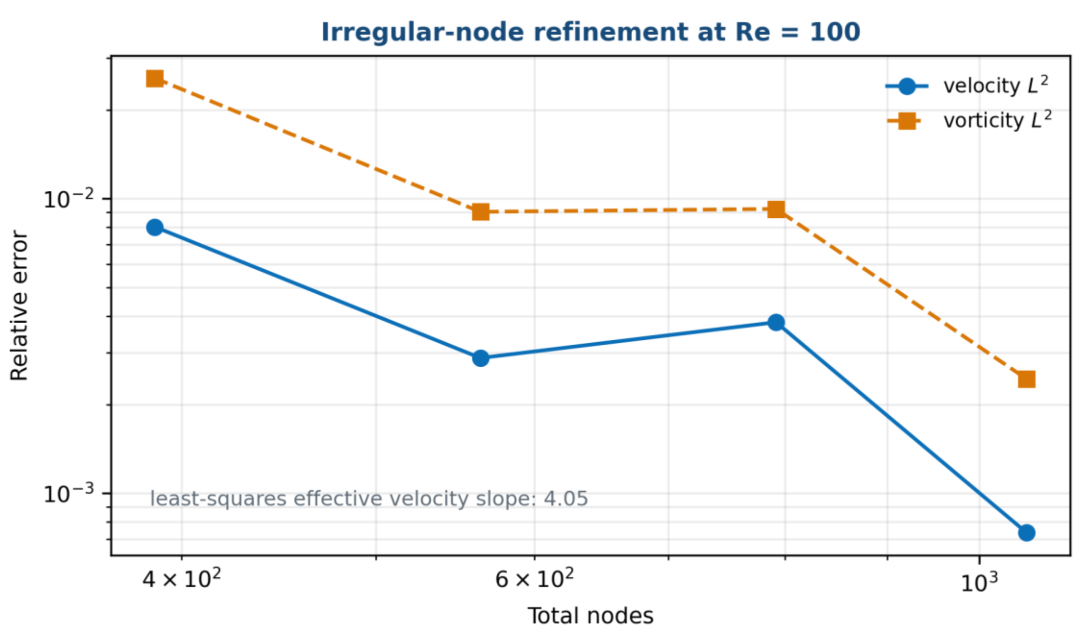

Figure 7. Refinement study at Re = 100. The intermediate nonmonotone point reflects irregular-stencil conditioning.

The relative velocity error was dropped by 90.84% for a total of 388 to 1056 nodes. The velocity error for the 792 node is larger than the one in the 564 node, the least-squares effective slope is 4.05. Therefore, the slope is not an established asymptotic order, it is merely an empirical description of the slope. The nonmonotonic point matches up with the local stencil geometry-sensitivity of strong-form RBF-FD [1, 18, 19].

Table 8. Five-seed irregular-cloud repeatability study at Re = 500 and 380 nodes.

Metric	Mean	Standard deviation	Minimum	Maximum
Velocity RMS error	0.051357	0.020859	0.029477	0.078761
Vorticity RMS error	0.134462	0.047809	0.078390	0.187110
Discrete divergence RMS	0.008227	0.001637	0.006734	0.010892

The mean of the velocity error for the five-seed is 5.14×10^{-2} and the standard deviation is 2.09×10^{-2}. The variation is too large to consider one single irregular cloud as representative of all. It emphasizes the importance of stencil quality diagnostics, oversampling and least-squares stabilization which were achieved in [19] and sets a well-defined statistical threshold on the matched-cloud results.

5.6 Interpretation relative to recent studies

The literature on the meshless Navier–Stokes [2]–[8] has shown that a divergence-free, stabilized approximation, locally adapted to the irregular geometry is possible without the use of conventional meshes. Two additional pressure prescribed diagnostics are introduced in the present study, that have typically not been included in those papers: one, a manufactured problem that is exactly invariant with respect to the pressure amplitude when using a filtered gradient, and the other, another algebraic mixed benchmark that is forced to annihilate compatible discrete gradients to roundoff. From this point of view, the study translates one of the main aspects of the pressure robust finite element results [9]–[17] into a local RBF-FD context.

The transfer will be not complete. Available mesh based tools consist of either an exact sequence, or of commuting projectors, or of an adjoint discrete gradient in a separate mixed diagnostic, together with symbolic curl filtering in the one branch, thus requiring two different diagnostics. Figuring out what went wrong with negative temperature, the analytic-gradient leaves no room for doubt in the necessity of letting a true general-purpose method include a commuting force projection. Similarly, the conditional stability theorem cannot be used in lieu of the more fundamental Reynolds–semi-robust estimates given in the work of [10], [11] and [14]. The present contribution is an integrated proof of concept, which can be reproduced, and the conditions of applicability are clearly presented.

5.7 Direct linkage between objectives and evidence

Table 9. Objective-to-evidence mapping.

Objective	Evidence	Direct result	Assessment
O1	Equations (6)–(10), Theorem 2, Table 3	Pressure amplitude changes to 10^6 leave velocity unchanged.	Achieved for the symbolically curl-filtered two-dimensional branch.
O2	Equations (30)–(32), Figures 2 and 4, Table 5	Adaptive nodes reduce matched-size velocity error by 67.0–88.7%.	Achieved for the Oseen stress test.
O3	Lemma 1, Propositions 1–2, Theorems 1–3	Compatibility and stability claims are stated with explicit assumptions.	Achieved conditionally; no unconditional Reynolds-uniform theorem.
O4	Tables 3–4, Figure 3	Compatible-gradient pollution reduced by more than 10^{15}; analytic sampling exposes projection gap.	Achieved and validity boundary identified.
O5	Tables 5–8, Figures 4–7	High-Re spatial errors, refinement, and five-seed variability are quantified.	Achieved as manufactured verification, not global-solver certification.
O6	Sections 2, 5.6, and 6	Results are interpreted against meshless and pressure-robust literature.	Achieved through critical comparison and limitations.

6. LIMITATIONS AND VALIDITY BOUNDARIES

- The nonlinear streamfunction–vorticity formulation is two-dimensional. The perforated-domain test uses manufactured boundary values; it does not solve general physical vorticity boundary closure.
- Exact mixed pressure invariance applies to loads represented in the compatible discrete gradient range. Independently sampled analytic gradients require a commuting load projection that is not yet implemented.
- The high-Re nonlinear tests use a near-exact initial iterate and therefore verify local spatial behavior rather than global convergence from arbitrary data.
- The Oseen comparison uses modest artificial viscosity at Re = 1000; although applied equally to both clouds, it prevents a claim of unstabilized high-Re robustness.
- Irregular-cloud repeatability exhibits substantial variation. Larger randomized studies, condition-number monitoring, and oversampled/least-squares RBF-FD variants are needed.
- The conditional stability and consistency statements depend on unisolvency, bounded local weights, coercivity/skew-adjointness, and local Jacobian nonsingularity. These properties are not proved for every possible cloud.
- The numerical experiments are manufactured-solution studies. Standard lid-driven cavity, backward-facing step, and cylinder-flow benchmarks should be added before claiming broad engineering performance.

7. Conclusions

An adaptive RBF-FD framework robust to the pressure was developed for the 2D incompressible Navier-Stokes analysis of irregular domains. It involves the use of curl-filtered streamfunction–vorticity equations, an adjoint-compatible mixed pressure-pollution diagnostic, PHS-plus-polynomial local differentiation, residual-driven node insertion, a stabilized Oseen stress test and damped Newton verification on a perforated domain.

The best one is the precise compatible load behavior. For pressure amplitudes up to 10^6, the curl-filtered velocity remained unchanged and the mixed discrete-gradient pollution coefficient decreased by a factor of 6.696e-02 to a maximum of 6.124e-17. The analytic-gradient control illustrates the reason for giving this challenge a fairly picky interpretation: Compatibility is not part of a solver's name.

Over a range of Re = 100–1000, placement of matched-size nodes with minimal placement error driven by the residual reduced velocity errors by up to 88.7–67.0%. The nonlinear 1056-node verification showed velocity errors less than 1.31×10-2 until a Reynolds number of 3200, but velocity error deterioration was found beginning with Re = 5000. The 1st to the last velocity error was reduced by 90.84% through the feature of refinement and the five-seed study clearly showed that the quality of irregular clouds has an influence on the accuracy.

The study thus offers a viable research line towards the Q1 instead of an ultimate universal solver. A commuting force projector for continuous loads, a primitive-variable nonlinear formulation with a provable discrete inf-sup / least-squares stability mechanism, adaptive stencil quality control, standard flow benchmarks and a three-dimensional compatible curl / Helmholtz implementation, are all next significant steps.

References

[1] A. Westermann, O. Davydov, A. Sokolov, and S. Turek, “Stability and accuracy of a meshless finite difference method for the Stokes equations,” International Journal for Numerical Methods in Engineering, vol. 126, no. 3, Art. no. e70000, 2025. doi: 10.1002/nme.70000

[2] X. Li, “A weak Galerkin meshless method for incompressible Navier–Stokes equations,” Journal of Computational and Applied Mathematics, vol. 445, Art. no. 115823, 2024. doi: 10.1016/j.cam.2024.115823

[3] X. Li and H. Dong, “Analysis of a divergence-free element-free Galerkin method for the Navier–Stokes equations,” Applied Numerical Mathematics, vol. 217, pp. 73–95, 2025. doi: 10.1016/j.apnum.2025.06.002

[4] D. L. Young, C.-L. Shih, L.-J. Yen, and C.-R. Chu, “Adaptive meshless local maximum-entropy finite element method for Navier–Stokes equations,” Journal of Mechanics, vol. 40, pp. 475–490, 2024. doi: 10.1093/jom/ufae039

[5] P. Jiang, H. Zheng, J. Xiong, and C. Zhang, “A stabilized local RBF collocation method for incompressible Navier–Stokes equations,” Computers & Fluids, vol. 265, Art. no. 105988, 2023. doi: 10.1016/j.compfluid.2023.105988

[6] M. Biglari and A. R. Soheili, “Efficient simulation of two-dimensional time-fractional Navier–Stokes equations using RBF-FD approach,” Engineering Analysis with Boundary Elements, vol. 160, pp. 134–159, 2024. doi: 10.1016/j.enganabound.2023.12.021

[7] Y. Liu and X. Wang, “A semi-Lagrangian meshfree Galerkin method for incompressible Navier–Stokes equations,” International Journal for Numerical Methods in Fluids, vol. 98, no. 3, pp. 177–196, 2026. doi: 10.1002/fld.70022

[8] A. Singh, I. F. Sbalzarini, and A. Obeidat, “Entropically damped artificial compressibility for the discretization corrected particle strength exchange method in incompressible fluid mechanics,” Computers & Fluids, vol. 267, Art. no. 106074, 2023. doi: 10.1016/j.compfluid.2023.106074

[9] D. A. Di Pietro, J. Droniou, and J. J. Qian, “A pressure-robust Discrete de Rham scheme for the Navier–Stokes equations,” Computer Methods in Applied Mechanics and Engineering, vol. 421, Art. no. 116765, 2024. doi: 10.1016/j.cma.2024.116765

[10] D. Castañón Quiroz and D. A. Di Pietro, “A Reynolds-semi-robust and pressure-robust Hybrid High-Order method for the time-dependent incompressible Navier–Stokes equations on general meshes,” Computer Methods in Applied Mechanics and Engineering, vol. 436, Art. no. 117660, 2025. doi: 10.1016/j.cma.2024.117660

[11] L. Beirão da Veiga, D. A. Di Pietro, J. Droniou, K. B. Haile, and T. J. Radley, “A Reynolds-semi-robust method with hybrid velocity and pressure for the unsteady incompressible Navier–Stokes equations,” SIAM Journal on Numerical Analysis, vol. 63, no. 6, pp. 2317–2342, 2025. doi: 10.1137/25M1736104

[12] V. Carlier, M. Campos Pinto, and F. Fambri, “Mass, momentum and energy preserving FEEC and broken-FEEC schemes for the incompressible Navier–Stokes equations,” IMA Journal of Numerical Analysis, vol. 45, no. 3, pp. 1868–1904, 2025. doi: 10.1093/imanum/drae047

[13] L. Beirão da Veiga, F. Dassi, and G. Vacca, “Pressure-robust SUPG-stabilized finite elements for the unsteady Navier–Stokes equation,” IMA Journal of Numerical Analysis, vol. 44, no. 2, pp. 710–750, 2024. doi: 10.1093/imanum/drad021

[14] B. García-Archilla and J. Novo, “Pressure and convection robust bounds for continuous interior penalty divergence-free finite element methods for the incompressible Navier–Stokes equations,” IMA Journal of Numerical Analysis, vol. 45, no. 1, pp. 163–187, 2025. doi: 10.1093/imanum/drad108

[15] N. Ahmed, G. R. Barrenechea, E. Burman, J. Guzmán, A. Linke, and C. Merdon, “A pressure-robust discretization of Oseen’s equation using stabilization in the vorticity equation,” SIAM Journal on Numerical Analysis, vol. 59, no. 5, pp. 2746–2774, 2021. doi: 10.1137/20M1351230

[16] A. Allendes, G. R. Barrenechea, and J. Novo, “A divergence-free stabilized finite element method for the evolutionary Navier–Stokes equations,” SIAM Journal on Scientific Computing, vol. 43, no. 6, pp. A3809–A3836, 2021. doi: 10.1137/21M1394709

[17] Y. Li, M. Feng, and Y. Bai, “Divergence-free stabilized virtual element method for the unsteady incompressible Navier–Stokes problem,” Journal of Computational and Applied Mathematics, vol. 473, Art. no. 116838, 2026. doi: 10.1016/j.cam.2025.116838

[18] M. E. Nielsen and B. Fornberg, “High-order numerical method for solving elliptic partial differential equations on unfitted node sets,” Computers & Mathematics with Applications, vol. 193, pp. 103–116, 2025. doi: 10.1016/j.camwa.2025.05.024

[19] I. Tominec, E. Larsson, and A. Heryudono, “A least squares radial basis function finite difference method with improved stability properties,” SIAM Journal on Scientific Computing, vol. 43, no. 2, pp. A1441–A1471, 2021. doi: 10.1137/20M1320079

[20] M. Jančič and G. Kosec, “Strong-form mesh-free hp-adaptive solution of a linear elasticity problem,” Engineering with Computers, vol. 40, pp. 1027–1047, 2024. doi: 10.1007/s00366-023-01843-6